NUMERICAL SOLUTION OF LIMITED-DATA INVERSE PROBLEMS ARISING FROM X-RAY TOMOGRAPHY AND ACOUSTIC INVERSE SCATTERING

ESA NIEMI

Academic dissertation

To be presented, with the permission of the Faculty of Science of the University of Helsinki, for public examination in Lecture Hall 2, Metsätalo Building, on June 24th, 2015, at 12 o'clock noon.

Department of Mathematics and Statistics
Faculty of Science
University of Helsinki

HELSINKI 2015

ISBN 978-951-51-1334-4 (paperback)
ISBN 978-951-51-1335-1 (PDF)
Unigrafia Oy
HELSINKI 2015

Acknowledgments

This work was done at the Department of Mathematics and Statistics, University of Helsinki, during the years 2010-2014.

I am deeply grateful to my advisors Samuli Siltanen and Matti Lassas, who made this work possible by providing a graduate student position, interesting research problems, excellent guidance and support. It has been a great privilege to have such scientists as supervisors. I also express my gratitude to Martin Burger and Oliver Dorn for the pre-examination of my thesis.

The articles of this thesis were written in co-operation with several colleagues; I thank all of them for fruitful collaboration. I also thank the Department of Mathematics and Statistics for pleasant and functional working environment. Special thanks go to IT specialist Martti Nikunen for prompt tech support on numerous occasions.

Finally, I thank Academy of Finland (Centre of Excellence programmes 213476 and 250215, project 134868 and project 141094) for financial support.

This thesis consists of an introduction and the following four articles:

[I] K. Hämäläinen, L. Harhanen, A. Hauptmann, A. Kallonen, E. Niemi and S. Siltanen **2014**, Total variation regularization for large-scale X-ray tomography. International Journal of Tomography and Simulation, Volume 25, Issue Number 1, 1–25.

[II] E. Niemi, M. Lassas and S. Siltanen **2013**, Dynamic X-ray tomography with multiple sources. 8th International Symposium on Image and Signal Processing and Analysis (ISPA2013), Trieste, Sept. 4-6, 618–621.

[III] E. Niemi, M. Lassas, A. Kallonen, L. Harhanen, K. Hämäläinen and S. Siltanen **2015**, Dynamic multi-source X-ray tomography using a spacetime level set method. Journal of Computational Physics, Volume 291, 218–237.

[IV] M. Ikehata, E. Niemi and S. Siltanen **2012**, Inverse obstacle scattering with limited-aperture data. Inverse Problems and Imaging, Volume 6, No. 1, 77–94.

The author had a major part in writing [II], [III] and [IV]. The author and A. Hauptmann were the principal writers of [I] with equal contribution. In addition, the author conducted the numerical studies in [II], [III] and [IV], and had an equal part with M. Lassas in the analysis in [III]. In [I] the numerical studies were conducted by the author and A. Hauptmann with equal contribution.

Contents

1 Introduction

Inverse problems arise from the need to interpret *indirect* measurements. For example, the problem of reconstructing the inner structure of a patient from her X-ray projection images is a classical example of an inverse problem.

Another example is the task of reconstructing an unknown object from the scattering pattern it produces for a certain input wave. In mathematical terms, consider a model expressed as

$$\mathcal{A}f = m, \tag{1}$$

where $\mathcal{A} : X \to Y$ is an operator between suitable model space X and data space Y. We call the problem of inverting (1), i.e. "given m, find f", an *inverse problem* provided that it violates at least one of the following conditions:

(i) there exists a solution,

(ii) there exists at most one solution, and

(iii) the solution depends continuously on the data.

According to Jacques Hadamard, a *well-posed* problem satisfies all the conditions (i)–(iii). Consequently, inverse problems, as considered in this work, are *ill-posed* problems.

From the view point of numerical solution of inverse problems, it is usually the violation of condition (iii), i.e. the lack of stability, that causes most difficulties. This comes from the fact that an actual measurement (data)

$$m_\delta = m + \epsilon, \quad \|\epsilon\| \leq \delta,$$

is usually contaminated by errors $\epsilon \neq 0$. Hence, even in the case that the inverse $\mathcal{A}^{-1}$ exists but is not continuous, the smallest errors in the data can cause arbitrarily large errors in the solution. To overcome this problem, some type of *regularization* method (or regularization strategy) is necessary for stabilizing the inversion.

Theoretically a regularization strategy is defined e.g. in [29] as a family of bounded (linear) mappings $\mathcal{R}_\alpha$, $\alpha > 0$, that approximate the inverse of $\mathcal{A}$ in the sense that

$$\lim_{\alpha \to 0} \mathcal{R}_\alpha \mathcal{A} f = f \quad \text{for all } f \text{ in the domain of } \mathcal{A}.$$

Moreover, the choice of $\alpha = \alpha(\delta)$ should depend on the noise level $\delta > 0$ such that $\alpha(\delta) \to 0$ and

$$\mathcal{R}_{\alpha(\delta)} m_\delta \to \mathcal{A}^{-1} m$$

as $\delta \to 0$, i.e. the regularized solution should tend to the true solution as the noise level tends to zero.

In a computational sense, one could say that an inverse problem is ill-posed because the contaminated data and the model do not contain sufficient information for solving the problem in a reasonable manner in practice. Hence, the idea of a computational regularization method can be seen as bringing some additional *a priori* information about the solution into the inversion.

As an example, let us consider one of the most classical regularization methods, Tikhonov regularization, which finds the solution of $\mathcal{A}f = m_\delta$ as the minimizer

$$\arg\min_f \{\|\mathcal{A}f - m_\delta\|^2 + \alpha\|f\|^2\}, \quad \alpha > 0.$$

Here the purpose of the first term of the objective functional is to ensure that the model $\mathcal{A}f = m_\delta$ is satisfied approximately, while the second term works for the prior information that the norm of the solution is not too large. The regularization parameter α is used to tune the balance between these two requirements.

Given an inverse problem that is ill-posed due to the lack of information, it is clear that reducing the data (indirect information about the unknown) will make the inversion even more difficult. Such limited-data cases are relevant to many practical applications and they arise e.g. from the need to minimize radiation dose in medical imaging or from the geometric restrictions in the measurement setting. The goal of this thesis was to develop and study novel computational inversion methods for such limited-data inverse problems in three cases: sparse-data stationary X-ray tomography, dynamic X-ray tomography with multiple fixed source-detector pairs and limited-aperture acoustic inverse obstacle scattering.

X-ray tomography problems are linear and (usually) only mildly ill-posed [39]. In contrast, inverse scattering problems are nonlinear and highly ill-posed [12]. Despite these facts, there is a surprising connection between the two problems; namely, the X-ray tomography can be seen as the limiting case $k \to \infty$ of the inverse scattering by inhomogeneous medium from an incident plane wave with frequency k, see [39].

The Introduction of this thesis is organized as follows. In Section 2 we describe the mathematical model of X-ray tomography (CT) and consider its limited-data applications: sparse-data (stationary) CT and dynamic multi-

source CT, both of which lead to a CT problem with sparse angular resolution. Section 3 discusses the problem of acoustic inverse obstacle scattering problem and its limited-aperture version. Section 4 reviews the basics of total variation regularization and discusses some of the computational challenges related to its numerical implementation. Section 5 explains the idea in level set methods and their application to solving inverse problems. Section 6 discusses Ikehata's enclosure method for inverse scattering problems. Finally, in Section 7 we review the main results of Publications I–IV.

2 Dynamic and sparse data X-ray tomography

X-rays revolutionized medical imaging soon after their discovery by Wilhelm Röntgen in 1895. They were first used by taking single X-ray projection images of a patient or target. A single projection image, however, gives only partial information about the target since the structures in depth dimension are lost/overlapped in the resulting projection image. The second revolution of X-ray imaging came in 1970s by the invention of X-ray tomography, or X-ray computed tomography (CT), an imaging methodology capable of producing a complete 2D or 3D reconstruction of the X-ray attenuation distribution inside the target. The pioneers of CT, Allan Cormack and Godfrey Hounsfield, won a 1979 Nobel prize for their work on CT.

Let us describe the linear mathematical model behind CT. Assume the X-ray attenuation at each point of $\Omega \subset \mathbb{R}^2$ or $\Omega \subset \mathbb{R}^3$ is modeled by the X-ray attenuation function $f : \Omega \to \mathbb{R}$. Let an X-ray travel through Ω on a straight line $L \subset \Omega$ and assume the initial and final intensities of the X-ray are $I_0(L)$ and $I_1(L)$, respectively. Then we have the following model based on the physics of X-radiation:

$$\int_L f(x)dx = -\log \frac{I_1(L)}{I_0(L)}. \tag{2}$$

The initial intensity $I_0(L)$ is known from the properties of the X-ray source while the final intensity $I_1(L)$ is measured using an X-ray detector. The ideal inverse problem of X-ray tomography is the following: given the intensities $I_1(L)$ of X-rays for all lines L through Ω, reconstruct the attenuation coefficient f. This is equivalent to solving f from

$$\mathcal{R}f = m,$$

where $\mathcal{R}$ is the Radon transform of f, defined in 2D by

$$\mathcal{R}f(L) = \mathcal{R}f(\theta, \sigma) = \int_L f(\mathbf{x}) d\mathbf{x}, \quad \mathbf{x} = (x, y),$$

with $L = L(\theta, \sigma) = \{(x, y) \in \mathbb{R}^2 : x \cos\theta + y \sin\theta = \sigma,\ \theta \in [0, \pi),\ \sigma \in \mathbb{R}\}$ and m is known from the X-ray measurements as explained above. This is a linear inverse problem and only mildly ill-posed, see [39].

In practice, of course, one has only a finite number of line integrals of f (measurements). Moreover, they are (most often) given in the form of projection images, either in parallel-beam, fan-beam or cone-beam geometry. For example, in the case that we have N equiangularly sampled parallel-beam projections, the model is of the form

$$\mathcal{R}f(\theta, \sigma) = m, \quad \theta \in \{0, \pi/N, 2\pi/N, \dots (N-1)\pi/N\},\ \sigma \in \mathbb{R}. \tag{3}$$

Assuming N, i.e. the angular resolution, is rather high, the so-called filtered-backprojection reconstruction algorithm (FBP) is the standard choice for computing the reconstruction, see [39, 27] for details.

In the following two subsections we consider the two CT problems studied in this thesis. Both of these lead to a problem where the number of projection images is highly limited.

2.1 Sparse-data X-ray tomography

As mentioned above, the standard choice for computing a CT reconstruction from an extensive set of projection images is FBP. There are, however, many applications where a tomographic reconstruction from angularly sparse CT data would be valuable. In these cases FBP might not lead to an optimal result. Examples of such applications include

- the need to minimize radiation dose to a patient in medical imaging, and
- dynamic X-ray tomography with multiple sources.

The latter of these is discussed in detail in the following subsection.

Mathematically the sparse-data CT problem is equivalent to the inversion of (3) with small N. An insight into the ill-posedness of this problem is given by [45], where it was shown that one can *stably* reconstruct the singularities

of f only in those directions θ for which the Radon transform is available. In other words, the less projections available, the less features (singularities) of f can be reconstructed in a well-posed manner without regularization. (To be precise, the analysis in [45] was done for the so-called limited-angle case assuming that $\mathcal{R}f(\theta, \sigma)$ is known for all θ in some open subset of S^1, but this can be "approximately" applied to the sparse-data case as well by considering the Radon transform in (3) is known for small neighborhoods of the directions θ.)

2.2 Dynamic X-ray tomography with multiple sources

Imaging of changing targets is difficult with usual CT imaging systems consisting of one rotating source-detector pair. Such modern CT machines used widely in hospitals today are capable of taking a complete set of projection images in about one second [28]. This one-second time is, however, too long when considering for example the imaging of a beating heart: a heart might go through a complete heartbeat during this time. To enable better temporal resolution, several approaches with multiple sources and/or detectors have been proposed, see for example [48, 52].

In this thesis a CT imaging setup with multiple fixed source-detector -pairs was considered, see Figures 1 and 2 for an illustration of possible measurement setups in 3D and 2D, respectively. Each of the source-detector -pairs take projection images simultaneously thus providing high temporal resolution; modern off-the-shelf X-ray detectors are able to take 400 or more frames per second. However, as is evident from the illustrations, the number of the source-detector -pairs possible to be used in a geometrically reasonable setup is rather limited. This means that the CT data available at a single time instant is inevitably sparse, which leads to a same type of ill-posedness issue as described in the previous subsection.

The mathematical model for such spatio-temporal CT imaging in 2+1 dimensions can simply be given by the Radon transform separately for each time instant. More precisely, let us model the two-dimensional object of interest at time t by a nonnegative X-ray attenuation function $w_t(x, y) = w(x, y, t) = w(\mathbf{x})$. Here $w : \Omega \subset \mathbb{R}^3 \to \mathbb{R}_+$ and

$$\mathcal{A}w = m, \tag{4}$$

where $\mathcal{A}$ is an operator consisting of a "stack" of standard 2D Radon trans-

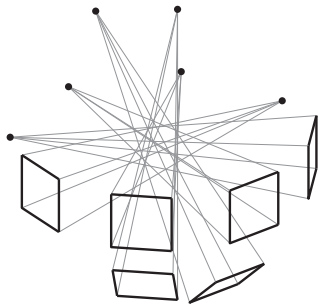

Figure 1: Example of a measurement setup with six x-ray sources and six detectors in three spatial dimensions. The sources are denoted by dots and the detectors by bold square-shaped frames.

forms $\mathcal{R}$,

$$(\mathcal{A}w)(L,t) := (\mathcal{R}w_t)(L) = \int_L w_t(x,y)dxdy.$$

Here $L = L(\theta,\sigma)$ denotes a line in the (x,y) -plane and the measurements $m = m(L,t)$ at fixed times are known from the X-ray measurements as described above. Finally, for later use we denote by E the set of all lines in the (x,y) -plane at different time instants.

3 Limited-data inverse obstacle scattering

Inverse obstacle scattering aims to extract information about distant and unknown targets using wave propagation. We consider the acoustic case where the target (or scatterer) is an impenetrable sound-hard obstacle $D \subset \mathbb{R}^2$ and the incident acoustic wave is a time-harmonic plane wave $e^{ikx\cdot d}$, $x \in \mathbb{R}^2 \setminus \overline{D}$, with incident direction $d \in S^1$ and wave number $k > 0$. Moreover, we assume that $D \subset \mathbb{R}^2$ is a bounded open set with Lipschitz boundary such that $\mathbb{R}^2 \setminus \overline{D}$ is connected, and we denote the unit outward normal to the boundary ∂D by ν. Then the resulting total wave field is the sum of the

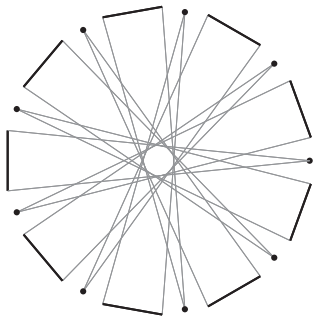

Figure 2: Example of a measurement setup with nine x-ray sources and nine detectors in two spatial dimensions. The sources are denoted by dots and the detectors by bold lines.

incident field and the scattered field w satisfying

$$\Delta w + k^2 w = 0 \quad \text{in } \mathbb{R}^2 \setminus \overline{D}, \tag{5}$$

$$\frac{\partial w}{\partial \nu} = -\frac{\partial}{\partial \nu} e^{ikx\cdot d} \quad \text{on } \partial D, \tag{6}$$

$$\lim_{r\to\infty} \sqrt{r}\left(\frac{\partial w}{\partial r} - ikw\right) = 0, \quad r = |x|. \tag{7}$$

It can be shown that this system has unique solution [17, 12]. Here the last equation (7) is called the Sommerfeld radiation condition. The above model arises for example as a cross-section of three-dimensional scattering from long cylindrical objects. The scattered field w can be shown to admit the asymptotic expansion

$$w(r\varphi) = \frac{e^{ikr}}{\sqrt{r}} F(\varphi; d, k) + O\left(\frac{1}{r^{3/2}}\right), \quad r \to \infty, \tag{8}$$

where the leading term $F(\varphi; d, k) \in \mathbb{C}$ is called the *far field pattern* of w. The far field pattern models scattering data measured far from the obstacle in direction $\varphi \in S^1$. The direct problem is to determine the far-field pattern for a given obstacle D.

For the inverse problem there are several possible cases that can be considered. For example, we might assume that $F(\varphi; d, k)$ is known for all $\varphi, d \in S^1$

or e.g. just for one $d \in S^1$. Moreover, we can aim to find the exact shape of the obstacle or just some partial information about it. The inverse problem considered in this thesis is the following: given the far field pattern $F(\varphi; d, k)$ for $\varphi \in \Gamma \subset S^1$ and for a single incident direction $d \in S^1$, find the convex hull of the obstacle. We refer to this problem as the limited-data or limited-aperture problem, since the far field pattern is known only for one d and only on a subset Γ of S^1.

The inverse scattering problem described above is nonlinear and highly ill-posed [12].

4 Total variation regularization for X-ray tomography

Rudin, Osher and Fatemi [49] introduced the idea of using total variation minimization for image denoising. They observed that minimizing the total variation of the image, rather than some of the more classical L^2 based penalties, enables better restoration of images containing sharp features and/or "blocky" textures. The same idea can be used for the regularization of an ill-posed equation $\mathcal{A}f = m$ by finding its solution as the minimizer of the functional

$$\mathcal{L}_{\mathrm{TV}}(f) := \|\mathcal{A}f - m\|_{L^2}^2 + \alpha \,\mathrm{TV}(f),$$

where $\mathrm{TV}(f)$ is the total variation of f and $\alpha > 0$ is a regularization parameter. This is known as total variation (TV) regularization and it is analyzed for example in [1]. In addition to noise removal, TV methods have been applied to recovering blurred noisy images [7, 55, 9, 4, 13].

One of the most interesting applications for TV regularization is X-ray tomography, especially sparse-data X-ray tomography. The artifacts typical to sparse-data tomographic reconstructions are known to be effectively reduced by TV regularization [33, 38, 41]. This suggests that the a priori information about the sparsity of the derivative of the reconstruction compensates well the sparsity of the CT data. Total variation regularization has been applied to tomographic problems for instance in [14, 33, 34, 51, 23, 53, 26, 54].

The main computational challenge of TV regularization is the non-differentiability of the objective functional. Another computational challenge, present especially in large-scale applications such as 3D X-ray tomography, is the computational cost of the minimization. One of the first solutions for over-

coming the first challenge was to smooth out the nondifferentiability of the TV penalty term and then apply some derivative-based optimization algorithm to the resulting discretized problem. If f is sufficiently smooth, we can write and approximate

$$\mathrm{TV}(f) = \|\nabla f\|_{L^1} = \int |\nabla f| \approx \int \sqrt{|\nabla f|^2 + \beta}$$

where $\beta > 0$ is a small parameter making the objective functional differentiable. After discretizing this problem, some optimization algorithm suitable for large-scale minimization, e.g. conjugate-gradient method or Barzilai-Borwein method, can be applied to obtain a numerical solution.

Several approaches not smoothing out the singularity of the TV functional have been proposed. One of them replaces the TV by a anisotropic approximation given by

$$\mathrm{TV}(f) = \int \sqrt{(\partial_1 f)^2 + (\partial_2 f)^2} \approx \int |\partial_1 f| + |\partial_2 f|,$$

after which the resulting minimization problem can be solved by standard quadratic programming methods [36, 31, 38].

Other methods for solving TV minimization problems include domain decomposition methods [21, 20], Bregman distance methods [42, 56, 22, 6, 57], primal-dual methods [8, 10, 16, 40], finite element methods [18, 2].

5 Level set methods and X-ray tomography

The original idea of level set methods is to represent an N -dimensional object by a level set of a real-valued implicit function (or level set function) of $N+1$ variables and to study e.g. the motion of the object using a PDE written for the implicit function [43]. This approach provides many computational advantages; for example, if the task is to model a moving surface whose topology changes during the motion, a level set method can take the changes easily into account without a need for reparametrizations. On the other hand, implicit function representation employs an excessive variable (dimension) which increases computational cost.

Level set methods can also be used for solving inverse problems such as inverse obstacle scattering [15, 50, 5]. The flexibility of the level set methods is very useful in these applications as well. For example, using an iterative

method for finding an obstacle D with explicit parametrization for the boundary ∂D would be difficult due to the possible topological changes during the iterations. Also, other common assumptions like "the obstacle D is star-like" might be necessary with conventional parametrized approaches. An iterative procedure formulated as a level set method avoids these difficulties.

A novel variant of level set methods was introduced in [32] for solving limited-data X-ray tomography problems. It was motivated by the idea that one

- first aims to find an approximation $\widetilde{\Omega}$ for the support of the attenuation function f, and
- then aims to find an attenuation function that is supported in $\widetilde{\Omega}$ and satisfies the CT model.

These two (mutually dependent) tasks were combined in a reconstruction procedure finding the minimizer as $g(\Phi(x,y))$, where $\Phi(x,y) := \lim_{s\to\infty}\phi(x,y,s)$ is the solution of the nonlinear (artificial) evolution equation

$$\begin{cases} \phi_s = -\mathcal{A}^*(\mathcal{A}(g(\phi)) - m) + \alpha\Delta\phi \\ (\nu\cdot\nabla - r)\phi|_{\partial\Omega} = 0 \end{cases} . \tag{9}$$

with a suitable initial condition $\phi(x,y,0) = \phi_0(x,y)$. Here $\mathcal{A}$ denotes the Radon transform, $\mathcal{A}^*$ is the transpose of $\mathcal{A}$, $r \geq 0$, $\alpha > 0$ is a regularization parameter and the function $g : \mathbb{R} \to \mathbb{R}$ is given by

$$g(\tau) = \begin{cases} \tau, & \text{if } \tau \geq 0 \\ 0, & \text{if } \tau < 0 \end{cases} . \tag{10}$$

The function $\phi(\cdot,\cdot,s)$ can be seen as a level set function; however, compared to classical level set methods, here $g(\phi)$ is used instead of $H(\phi)$ (H is the Heaviside function), i.e. the attenuation inside the level set $\{\phi = 0\}$ is given by the level set function itself, not by a constant. As explained in [32] and also in Section 7.3 below, the evolution equation above is motivated by the minimization of the functional

$$\|\mathcal{A}g(u) - m\|_2^2 + \alpha\|\nabla u\|_2^2.$$

In other words, the reconstruction method makes use not only of the level set motivated ideas explained above, but also of the a priori information that the gradient of the attenuation function is not too large. We finally remark here that using g instead of the Heaviside function H also makes the analysis of the evolution equation (9) easier, see [32].

6 Enclosure method for inverse scattering

Many different solution methods for inverse (obstacle) scattering problems have been proposed. Perhaps the simplest of those are based on a linear approximation of the originally nonlinear problem or on nonlinear optimization methods, see [12]. The former of these has the disadvantage of neglecting the nonlinear nature of the problem, for example multiple scattering. The latter, on the other hand, requires information about the unknown that is in general not available.

More advanced methods include the linear sampling method [11], the factorization method [30] and the method of singular sources [46]. These methods are often called "sampling methods" since each of them determines if a point z belongs to the obstacle by studying certain property related to the so-called far field operator and a function depending on z. All these methods require the knowledge of the far field pattern for several incident and several observation directions.

The limited-aperture inverse obstacle scattering problem described in Section 3 makes use of only one incident direction. This rules out the sampling methods described above. On the other hand, one could apply the nonlinear optimization method. Other methods for such limited aperture problem includes the *no response test* [37], the *range test* [44] and the enclosure method [25, 24].

The version of the enclosure method studied in Publication IV was proposed in [24]. The term "enclosure method" comes from the fact that the method aims to find the convex hull of the obstacle $D \subset \mathbb{R}^2$, i.e. the goal is to determine the function $h_D : S^1 \to \mathbb{R}$,

$$h_D(\omega) := \sup_{x \in D} \; x \cdot \omega, \tag{11}$$

whose knowledge gives us the convex hull of D, see Figure 3 for an illustration. A crucial assumption behind the theory of the method is that D is polygonal, i.e. D consists of a finite collection of polygons D_j satisfying $\overline{D}_j \cap \overline{D}_{j'} = \emptyset$ for $j \neq j'$ and that the directions $\omega \in S^1$, for which the value of h_D is computed, are regular, i.e. the set $\{x \in \mathbb{R}^2 : x \cdot \omega = h_D(\omega)\} \cap \partial D$ contains only one point, see Figure 3. Then, identifying any point $z = (z_1, z_2) \in \mathbb{R}^2$ with the complex number $z_1 + iz_2$ and defining the density

$$g_N(\varphi; \tau, k, \omega) := \frac{1}{2\pi} \sum_{|\ell| \leq N} \left(\frac{ik\varphi}{(\tau + \sqrt{\tau^2 + k^2})\omega} \right)^{\ell} \tag{12}$$

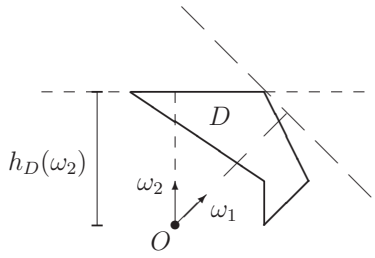

Figure 3: A polygonal obstacle D, a regular direction ω_1 with respect to D, a non-regular direction ω_2 with respect to D, and the value $h_D(\omega_2)$ of the support function for direction ω_2.

and the indicator function

$$I_\omega(\tau) := \log \left| \int_{S^1} F(-\varphi; d, k) g_N(\varphi; \tau, k, \omega) d\sigma \right|,$$

one can show ([24]) that with an appropriate choice of $\tau = \tau(N) \xrightarrow[N\to\infty]{} \infty$

$$\frac{1}{\tau} I_\omega(\tau) \to h_D(\omega), \quad N \to \infty. \tag{13}$$

Moreover, in the case that the far field pattern $F(\varphi; d, k)$ is known only for $\varphi \in \Gamma \subset S^1$, where Γ is a proper open subset of S^1, it was shown in [24] that a formula similar to (13) holds for a limited-aperture density g_N given by a truncation of the formal solution of the integral equation

$$\int_{-\Gamma} e^{ikx\cdot\varphi} g(\varphi) d\sigma = e^{x\cdot(\omega + i\sqrt{\tau^2+k^2}\omega^\perp)}, \quad x \in \mathbb{R}^2, \tag{14}$$

where $\omega^\perp = (\omega_1, \omega_2)^\perp = (\omega_2, -\omega_1)$. In Publication IV an *explicit* formula for such a limited-aperture density g_N was derived and a numerical algorithm based on that density was introduced and studied numerically using simulated far field data.

7 Review of results in Publications I–IV

In this section we briefly review the main ideas and results in Publications I–IV.

7.1 Publication I

As discussed in Section 2.1, sparse-data tomography problems, arising for example from the need to minimize the radiation dose in medical applications, call for advanced reconstruction algorithms. Total variation regularization (TV) has turned out to be an interesting option for such problems, see e.g. [33, 38]. Further regularization can be obtained by requiring the solution to be non-negative, i.e. by making use of the fact that the intensity of the X-rays cannot increase during their travel from the X-ray source to the detector. A computational method for solving such TV problems with non-negativity constraints, i.e.

$$\min_{f \geq 0} \mathcal{L}_{TV}(f) := \|\mathcal{A}f - m\|_{L^2}^2 + \alpha TV(f) \tag{15}$$

with f, m and the Radon transform $\mathcal{A} = \mathcal{R}$ as described in Section 2, is introduced in Publication I. The new method is called *discontinuity-based projected subgradient descent* (DB-PSGD). It employs a discretization scheme inspired by discontinuous Galerkin methods and a subgradient descent algorithm for minimization. This new computational method was tested numerically with both simulated and real X-ray data. Moreover, another recent method known as projected Barzilai-Borwein (PBB) for solving (15) approximately, was applied here to real X-ray data for the first time.

7.1.1 Computational methods

Since the main work of the author in this paper was on the PBB method and on the numerical computations with real X-ray data, we only briefly discuss the DB-PSGD method here. DB-PSGD is motivated by discontinuous Galerkin methods. More precisely, it is based on dividing the TV term into (i) the TV of the "continuous parts" and (ii) the jump part, i.e.

$$TV(f) = \int_J |f^+ - f^-| ds + \sum_{k=1}^{N} \int_{T_k} |\nabla f| dx.$$

Here the domain $\Omega \subset \mathbb{R}^2$ of f is discretized into pixels $T_1, \ldots, T_N$, $N = n \cdot n$, as shown in Figure 1 of Publication I, J denotes all the boundaries between the pixels $T_1, \ldots, T_k$, and f^+ and f^- denote, roughly speaking, the values of f on the different sides of the pixel boundary. We approximate f by the vector $\mathbf{f} = [\mathrm{f}_1, \ldots, \mathrm{f}_N]$, where each component f_j approximates the value of f

in pixel T_j. The resulting minimization problem is solved by a subgradient descent scheme leading to the iteration

$$\mathbf{f}^{k+1} = P(\mathbf{f}^k - \lambda_k \Delta \mathbf{f}^k), \quad k = 0, 1, 2, \ldots, \tag{16}$$

where $\mathbf{f}^k = [(\mathrm{f}^k)_1, (\mathrm{f}^k)_2, \ldots, (\mathrm{f}^k)_N] \in \mathbb{R}^N$, P is a projection operator to the feasible region $\mathbf{f} \geq 0$,

$$\big(P(\mathbf{f})\big)_j := \begin{cases} \mathrm{f}_j & \text{if } \mathrm{f}_j \geq 0 \\ 0 & \text{if } \mathrm{f}_j < 0 \end{cases}, \tag{17}$$

and $\Delta \mathbf{f}$ is given by

$$\Delta \mathbf{f} = 2A^T(A\mathbf{f} - \mathbf{m}) - \alpha \left(D_1^T \frac{D_1 \mathbf{f}}{|D_1 \mathbf{f}|} + D_2^T \frac{D_2 \mathbf{f}}{|D_2 \mathbf{f}|} \right) + \alpha\big((D_1 + D_2 + D_1^T + D_2^T)\mathbf{f}\big), \tag{18}$$

with the matrix $A \in \mathbb{R}^{M \times N}$ approximating the operator $\mathcal{A}$ and the vector $\mathbf{m} \in \mathbb{R}^M$ known from the X-ray measurements. The matrices $D_1, D_2 \in \mathbb{R}^{N \times N}$ denote the finite difference matrices in horizontal and vertical directions, respectively. The absolute values and divisions are taken element-wise, and in the case that the ith element $(D_j \mathbf{f})_i = 0$, we define $\left(D_j^T \frac{D_j \mathbf{f}}{|D_j \mathbf{f}|} \right)_i = 0$ $(j = 1, 2)$.

As an additional interesting remark we note here that the last term in (18) is a finite difference approximation of the Laplace operation Δf, i.e. one can see (16) as a minimization scheme for finding the minimizer of

$$\mathcal{L}_{TV}(f) + \alpha \|\nabla f\|_{L^2}^2.$$

Hence, DB-PSGD penalizes not only the total variation of the function but also the 2-norm of its gradient.

The step size λ_k in (16) is determined by

$$\lambda_k = \min \left\{ \lambda_{\max},\ \max \left\{ \lambda_{\min},\ \left\{ \lambda \in \mathrm{FR}_\lambda :\ \lambda = \frac{\lambda_{k-1}}{2^j},\ j \geq -1 \right\} \right\} \right\}, \tag{19}$$

where

$$\mathrm{FR}_\lambda := \left\{ \lambda : L(\mathbf{f}^{k+1}) < L(\mathbf{f}^k),\ \mathbf{f}^{k+1} = \mathbf{f}^k - \lambda \mathbf{f}^k \right\},$$

with $L : \mathbb{R}^N \to \mathbb{R}$ the discretized version

$$L(\mathbf{f}) := \|A\mathbf{f} - \mathbf{m}\|_2^2 + \alpha \|\tilde{D}\mathbf{f}\|_1 \tag{20}$$

of the functional $\mathcal{L}$. Here $\tilde{D}$ is the approximation of the Euclidean norm of the gradient of f, the jth component given by

$$(\tilde{D}\mathbf{f})_j = \sqrt{(\mathrm{f}_{j+n} - \mathrm{f}_j)^2 + (\mathrm{f}_{j+1} - \mathrm{f}_j)^2} \tag{21}$$

with the zero Neumann boundary condition applied for the boundary pixels.

The PBB method on the other hand is a projected version of the gradient-based Barzilai-Borwein (BB) optimization method [3] that assumes the objective functional to be differential. It was applied to a differentiable approximation of L given by

$$L_\beta(\mathbf{f}) := \|A\mathbf{f} - \mathbf{g}\|_2^2 + \alpha\|\tilde{D}\mathbf{f}\|_{1,\beta},$$

where

$$\|\mathbf{f}\|_{1,\beta} := \sum_{j=1}^{N} \sqrt{\mathrm{f}_j^2 + \beta}, \quad \mathbf{f} = (\mathrm{f}_1, \ldots, \mathrm{f}_N) \in \mathbb{R}^N$$

and $\beta > 0$ is a small smoothing parameter. The resulting iteration is of the form

$$\mathbf{f}^{k+1} = P(\mathbf{f}^k - \lambda_k \nabla L_\beta(\mathbf{f}^k))$$

where the step size is computed as

$$\lambda_k = \frac{(\mathbf{f}^k - \mathbf{f}^{k-1})^T(\mathbf{f}^k - \mathbf{f}^{k-1})}{(\mathbf{f}^k - \mathbf{f}^{k-1})^T(\nabla L_\beta(\mathbf{f}^k) - \nabla L_\beta(\mathbf{f}^{k-1}))}. \tag{22}$$

The advantages of the BB (or PBB) method are (i) low-cost matrix-free operations, (ii) better convergence properties than in the classical steepest descent method [19], and (iii) possibility to ensure convergence by employing a simple globalization strategy [47].

7.1.2 X-ray data from a walnut

The two computational methods described in the previous subsection were tested numerically with both simulated data and real X-ray data of a walnut. An illustration of the measurement system is shown in Figure 4. The original 3D cone-beam measurement setup was reduced to 2D by taking the fan-beam sinogram corresponding to the central cross-section of the walnut to serve as the test data.

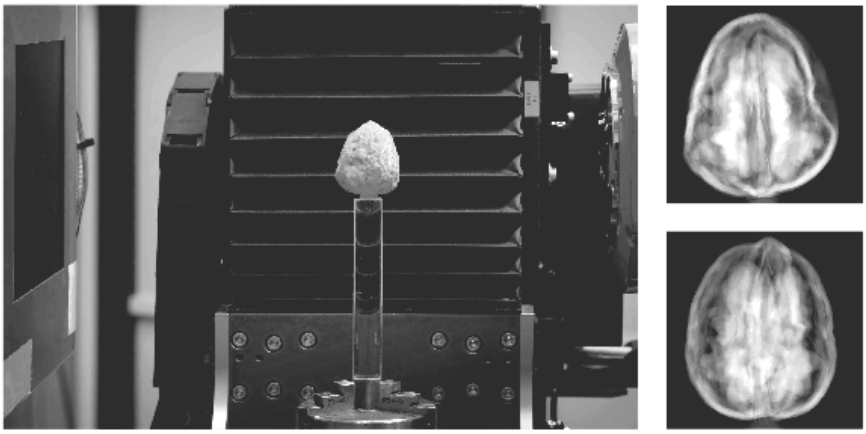

Figure 4: Left: Experimental setup for collecting tomographic X-ray data of a walnut. The detector plane is on the left and the X-ray source on the right in the picture. The walnut is attached to a computer-controlled rotator platform. Right: Two examples of the resulting projection images.

7.1.3 Numerical results

The numerical experiments aimed to compare the quality of the reconstructions and computation times of the two methods. As suggested by the computational algorithms, a single iteration with PBB is faster to compute than a single iteration with DB-PSGD. More precisely, an iteration with PBB is approximately twice as fast as that with DB-PSGD. However, as indicated by the example in Figure 5, it is not only the matter of the CPU time of a single iteration but also the convergence speed. In this example it seems that DB-PSGD converges to the correct solution much faster than PBB (with the chosen metrics). Indeed, to obtain a relative L^2 error of less than 50% takes about 50 iterations with DB-PSGD while PBB requires 150-200 iterations. Same type of conclusion may be drawn from the actual reconstructions shown in Figure 2 of Publication I.

In terms of quality of the reconstruction, as evaluated by visual inspection, the difference between the two methods is not so large, yet one could argue that DB-PSGD seems to produce somewhat sharper reconstructions, see e.g. Figure 6.

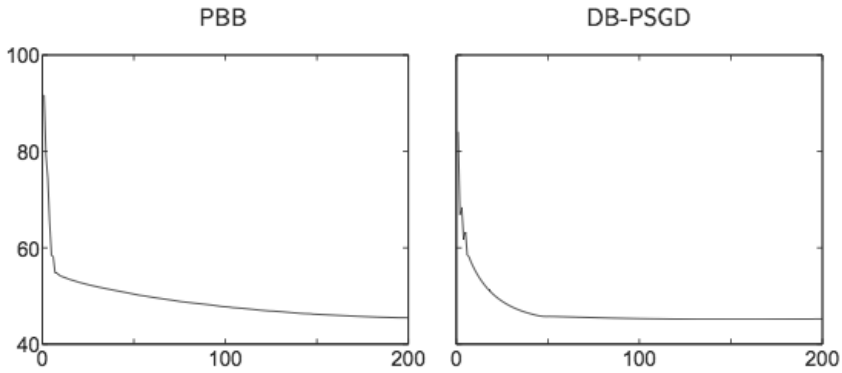

Figure 5: Relative L^2 errors of the PBB and DB-PSGD reconstructions as function of iterations. Here the test data was simulated data for Shepp-Logan phantom in resolution 512×512, 20 projecttion images and 2% noise level.

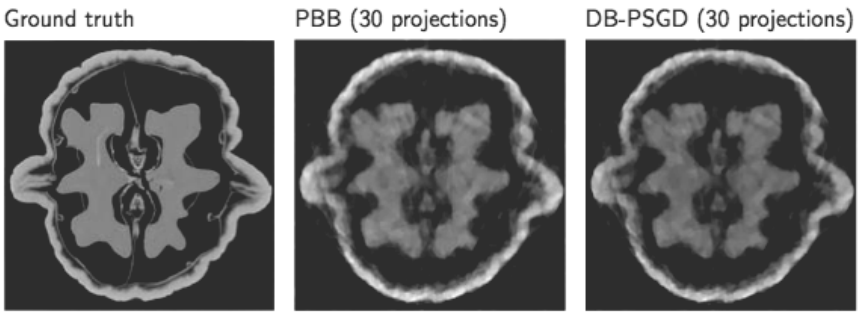

Figure 6: Reconstructions of a walnut from 30 fan-beam projections

7.2 Publication II

As discussed in Section 2.2, dynamic X-ray tomography with multiple fixed-position sources leads to sparse angular resolution at a single time step while the attainable temporal resolution is high. In this work we developed a computational method for such CT problems by generalizing the modified level set method introduced in [32] to time-dependent setting by adding time as an additional variable to the level set function. The new method was tested numerically with simulated (2+1) -dimensional CT data.

7.2.1 Space-time level set method for dynamic CT

Because of the low angular and high temporal resolution in dynamic multi-source CT, we aimed at developing an algorithm that

1. suppresses effectively the artifacts produced by angular sparsity of the CT data, and

2. makes use of the high temporal resolution by enforcing regularity (of the reconstruction) in time.

As discussed in Section 5, numerical evidence suggests that the modified level set method introduced and studied in [32] effectively reduces the artifacts natural to sparse data CT reconstructions. In this work we introduced the idea of extending the method to the time-dependent setting by taking time t as third variable to the level set function, see Figure 7. More precisely, we find the reconstruction in the form $w(x, y, t) = g(\Phi(x, y, t))$, where g is as defined in (10) and $\Phi(x, y, t) := \lim_{s\to\infty} \phi(x, y, t, s)$ is the steady state solution of the evolution equation

$$\begin{cases} \phi_s(x, y, t, s) = -\mathcal{A}^*(\mathcal{A}(g(\phi(x, y, t, s))) - m) + \alpha\Delta\phi(x, y, t, s) \\ (\nu \cdot \nabla - r)\phi(x, y, t, s)|_{\partial\Omega} = 0 \end{cases} \tag{23}$$

with a suitable initial condition $\phi(x, y, t, 0) = \phi_0(x, y, t)$. Here $\mathcal{A}$ is as defined in Section 2.2, $\mathcal{A}^*$ denotes the transpose of $\mathcal{A}$, $\alpha > 0$ is a regularization parameter, $r \geq 0$, and the Laplace operator includes derivatives in t, that is $\Delta\phi = \phi_{xx} + \phi_{yy} + \phi_{tt}$.

This approach can be seen as a generalization of level set methods (see [32]) with the evolution equation based on minimizing the slightly modified generalized Tikhonov functional,

$$\arg\min_u \left\{ \|\mathcal{A}g(u) - m\|_2^2 + \alpha\|\nabla u\|_2^2 \right\}. \tag{24}$$

Compared to classical level set methods, we use g instead of the Heaviside function in (23) and in (24). This means that inside the level set we represent the attenuation coefficient by the level set function itself (not by a constant). On the other hand, g is smoother than the Heaviside function, which makes analysis of (23) easier, see [32].

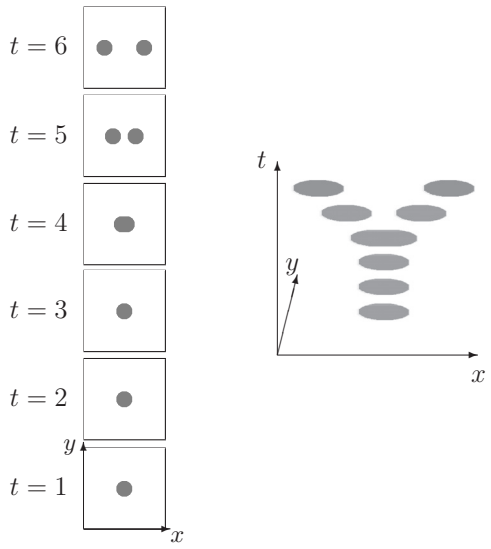

Figure 7: Illustration of the idea in 2+1 -dimensional spatio-temporal interpretation. *Left*: six states $v_t = v_t(x, y)$ of a dynamic 2-D object at $t = 1, \ldots, 6$. *Right*: the same dynamic object considered in three-dimensional Euclidean (x, y, t) -space as $v = v(x, y, t)$.

7.2.2 Numerical example

Let us then look at a numerical example in Figure 8. The measurement setting in this example makes use of nine source-detector pairs as shown in Figure 2. The "Generalized Tikhonov" refers to 2D reconstructions computed separately for each 2D slice using Tikhonov regularization with the standard regularization function $\|\cdot\|$ replaced by $\|\nabla(\cdot)\|$, i.e. penalizing the norm of the gradient of the function instead of the norm of the function.

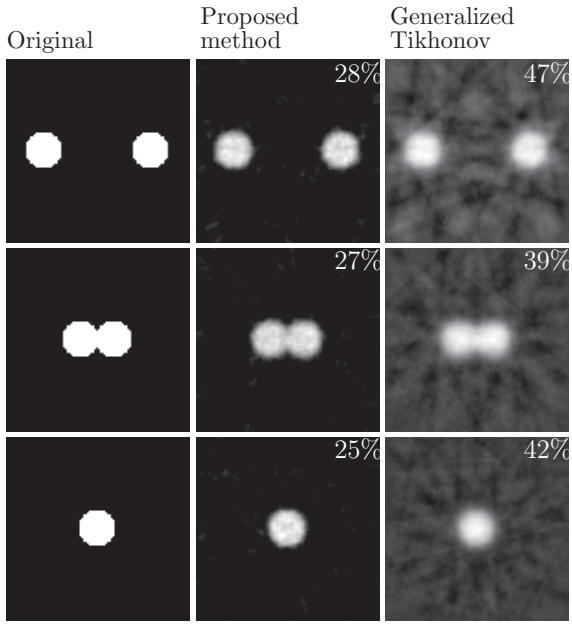

Figure 8: Reconstructions of the Y-shaped object at three different stages. The relative L^2 errors are shown in the upper right corners of the reconstructions. 5% added Gaussian random noise in the data.

The test phantom was a similar "Y-shaped" object in space-time as shown in Figure 7 but with finer in resolution; the overall (x, y, t) -resolution in the demo is $100 \times 100 \times 100$. The evolution equation (23) was solved using Euler's method with 50 steps, and the initial state $\phi_0 \equiv 0$. The computation times of the two methods were practically the same. Compared to the rather standard generalized Tikhonov regularization, the proposed method seems to give reconstructions with smaller L^2 errors and closer to the original object as judged by visual inspection as well.

7.3 Publication III

The dynamic multi-source CT reconstruction method introduced and studied in this work is essentially a generalization of the method in Publication II. More precisely, instead of regularizing only the first derivative of the re-

construction as in Publication II, here the L^2 norms of up to $n \in \{1, 2, \ldots\}$ derivatives are included in the regularization term. The main new contributions of this work are (i) a proof of a connection between the case $n = 1$ and standard Tikhonov regularization, (ii) an existence result for the case $n \geq 2$ and (iii) application of the new method with $n = 2$ to simulated and real 2+1 -dimensional X-ray data.

7.3.1 The new space-time level set method

As discussed above, the modified space-time level set method introduced in Publication II is based on the minimization of the functional

$$F_1(u) = \frac{1}{2}\|\mathcal{A}g(u) - m\|^2_{L^2(E)} + \frac{\alpha}{2}\|\nabla u\|^2_{L^2(\Omega)}, \tag{25}$$

where $\mathcal{A}, m, E$ and Ω are as explained in Section 2.2, g is defined in (10) and $\alpha > 0$ is a regularization parameter. In this work we generalized the approach by allowing more derivatives of u in the regularization part, i.e. we essentially studied the minimization of the functional

$$F_n(u) = \frac{1}{2}\|\mathcal{A}g(u) - m\|^2_{L^2(E)} + \frac{\alpha}{2}\sum_{1\leq|\beta|\leq n}\|D^\beta u\|^2_{L^2(\Omega)}, \tag{26}$$

where $n \in \{1, 2, \ldots\}$ and β is a multi-index. In the level set terminology, we call a minimizer v of F_n a level set function and consider $g(v)$ as the reconstruction. Note that the case $n = 1$ is equivalent to (25) and hence equivalent to the method in Publication II.

We established two theoretical results concerning the minimization of F_n. The first one of these shows that the minimization of F_1 is essentially equivalent to the non-negativity constrained Tikhonov problem

$$\operatorname*{arg\,min}_{u\in H^1, u\geq 0}\left\{\frac{1}{2}\|\mathcal{A}u - m\|^2_{L^2(E)} + \frac{\alpha}{2}\|\nabla u\|^2_{L^2(\Omega)}\right\}, \tag{27}$$

which has a unique minimizer. This result gives new insight into the connection between level set methods and classical Tikhonov regularization. On the other hand, it explains our numerical observations that the level set function for $n = 1$ never attains very negative values.

The second result established the existence of a global minimizer of F_n for $n \geq 2$. Due to the nonlinearity caused by function g, the functional

F_n is neither convex nor coercive. Thus we needed to employ rather non-standard arguments for the existence proof. In particular, we made the following assumptions regarding the signal-to-noise ratio and the size of the regularization parameter $\alpha > 0$. We assumed the signal-to-noise ratio in the measurement is $M > 2$, i.e. the true model being $m^* = \mathcal{A}u^*$, the error ϵ in the measured data $m = m^* + \epsilon$ satisfies

$$\|\epsilon\|_{L^2(E)} \leq \frac{1}{M}\|m^*\|_{L^2(E)}.$$

In addition, we assumed that the regularization parameter $\alpha \in (0, \alpha_0)$, where $\alpha_0 = \alpha_0(u^*, m^*, M)$ satisfies

$$\frac{M-2}{M}\|m^*\|^2_{L^2(E)} = \alpha_0(u^*, m^*, M) \sum_{1\leq|\beta|\leq n} \|D^\beta u^*\|^2_{L^2(\Omega)}.$$

Under these assumptions we were able to prove that F_n has a global minimizer.

7.3.2 Numerical computations and data

Proposed level set reconstruction algorithm with $n = 2$. As the case $n = 1$ leads to the well-known Tikhonov problem, it is convenient to compute the reconstruction for $n = 1$ as the minimizer (27). For $n = 2$ no such result exists, and thus we developed and studied a new numerical algorithm for computing reconstructions with $n = 2$. For simplicity we dropped the mixed derivatives from the functional F_2 and proposed a computational algorithm for minimizing

$$\|\mathcal{A}g(u) - m\|^2_{L^2(E)} + \alpha\left(\|\nabla u\|^2_{L^2(\Omega)} + \|\partial_x^2 u\|^2_{L^2(\Omega)} + \|\partial_y^2 u\|^2_{L^2(\Omega)} + \|\partial_t^2 u\|^2_{L^2(\Omega)}\right).$$

Since this functional is not differentiable due to the singularity of g at zero, we replaced g by the following differentiable approximation

$$g_\delta(\tau) = \begin{cases} \sqrt{\tau^2+\delta^2} - \delta, & \text{if } \tau > 0, \\ 0, & \text{if } \tau \leq 0, \end{cases}, \tag{28}$$

where $\delta > 0$ is a small parameter. After this modification, we applied the gradient-based optimization method of Barzilai and Borwein for minimizing the resulting discretized problem. Having found a minimizer, we projected it

to the nonnegative quadrant of the Euclidean space to obtain the space-time level set reconstruction.

Let us make a few additional remarks on the algorithm. The second derivatives of u were approximated by central difference approximations with unit spacing in spatial (x, y) directions and with spacing $h_t > 0$ in temporal direction. The spacing h_t can be chosen rather freely but it may have a significant effect on the reconstructions; larger h_t means less regularization in temporal direction while smaller h_t means more regularization in temporal direction. In the numerical examples of this work we chose h_t to be approximately of the same magnitude as the spatial changes in the 2D target between two consecutive time steps. On the boundary $\partial\Omega$ we employed the condition $u|_{\partial\Omega} = -1$, since ideally we would like to have the level set function to be negative outside the level set $\{(x, y, t) : u(x, y, t) > 0\}$.

X-ray data. The proposed space-time level set method was tested with two simulated test cases and one real X-ray data test case. Here we consider one of the two simulated cases. The phantom is shown at the top of Figure 9. Using a spatio-temporal (x, y, t) resolution of $100 \times 100 \times 100$, seven fan-beam projections were simulated at each time step and 5% Gaussian random noise was added to demonstrate errors in the data.

A real 2+1 -dimensional CT data set was collected using the cone-beam CT device shown in Figure 4 and a set of sugar cubes as follows. The sugar cubes were positioned into 10 different formations on a plate and each of these formations was measured with the CT device by taking a set of 120 projection images with 3 degree angular step. From these data the 10 fan-beam sinograms corresponding to the central slice of the sugar cubes were taken to serve as the 2+1 -dimensional test data. Ten of those fan-beam projections (36 degree angular step) were used for testing the proposed space-time level set reconstruction algorithm; the full set of 120 fan-beam projections was used only for computing ground truth reconstructions.

7.3.3 Reconstructions from X-ray data

Let us finally take a look at the reconstructions obtained by applying the proposed space-time level set algorithm with $n = 2$ to the simulated and real X-ray data described above. The reconstructions computed from the simulated data are shown in Figure 9, while the real data sugar cube reconstructions can be found in Figures 10 and 11; the first five of the ten 2D reconstructions

of the sugar cubes are shown in Figure 10 and the last five in Figure 11. The spatial resolution in the reconstructions is 256×256. The ground truth reconstructions of the sugar cubes were computed from the larger sets of 120 projections while the actual reconstructions only made use of 10 projections per time step. For comparison, we show also the corresponding space-time level set reconstructions with $n = 1$ and the corresponding 2D total variation reconstructions. The former of these were computed simply as the minimizer (27). The total variation method applied no temporal smoothing but computed each 2D reconstruction separately from the CT data measured at that time.

In addition to the separate 2D reconstructions of the sugar cubes, an isosurface image of the $n = 2$ level set reconstruction in space-time is shown in Figure 12.

These results indicate that the proposed method with $n = 2$ yields reconstructions that are superior to the standard Tikhonov ($n = 1$) and favorably comparable to those of total variation regularization.

7.4 Publication IV

This work studied limited-aperture acoustic inverse obstacle scattering, where one sends a *single* incident time-harmonic plane wave towards the area of interest and measures the scattered field in all or only in limited directions, see Section 3 for details. A novel computational algorithm (a variant of the *enclosure method*) for recovering the convex hull of the sound-hard obstacle from noisy limited-aperture far-field data was introduced and studied numerically by simulated examples.

7.4.1 The enclosure method

The optimal solution to an inverse obstacle scattering problem would be the complete shape of the obstacle. In this work we were interested in a variant of the enclosure method whose aim is to only find the convex hull of the obstacle, as explained in Section 6. More precisely, we aim to determine the support function h_D defined in (11) from the knowledge of the far field pattern $F(\varphi; d, k)$ for fixed $k > 0$ and $d \in S^1$ and $\varphi \in \Gamma \subset S^1$. We refer to Γ as the *aperture*.

Our approach for solving the inverse problem is based on the behavior of

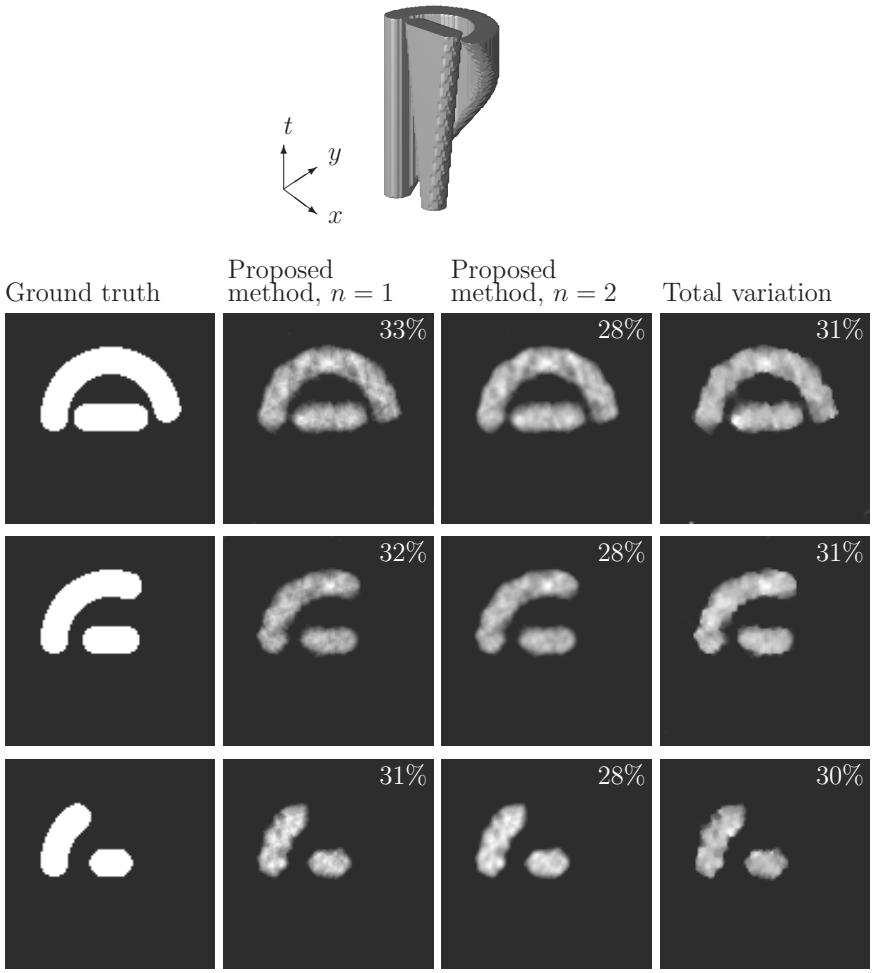

Figure 9: *Top:* An isosurface image of the simulated, dynamic 2D phantom in space-time. The attenuation is constant one inside the isosurface and zero outside. *Three lowest rows:* Three different states/reconstructions of the dynamic 2D phantom. The relative errors of the reconstructions with respect to the 2-norm are given in the upper right corners of the reconstructions. Overall spatio-temporal resolution is $100 \times 100 \times 100$. The number of fan-beam projections at a single time step is seven (7).

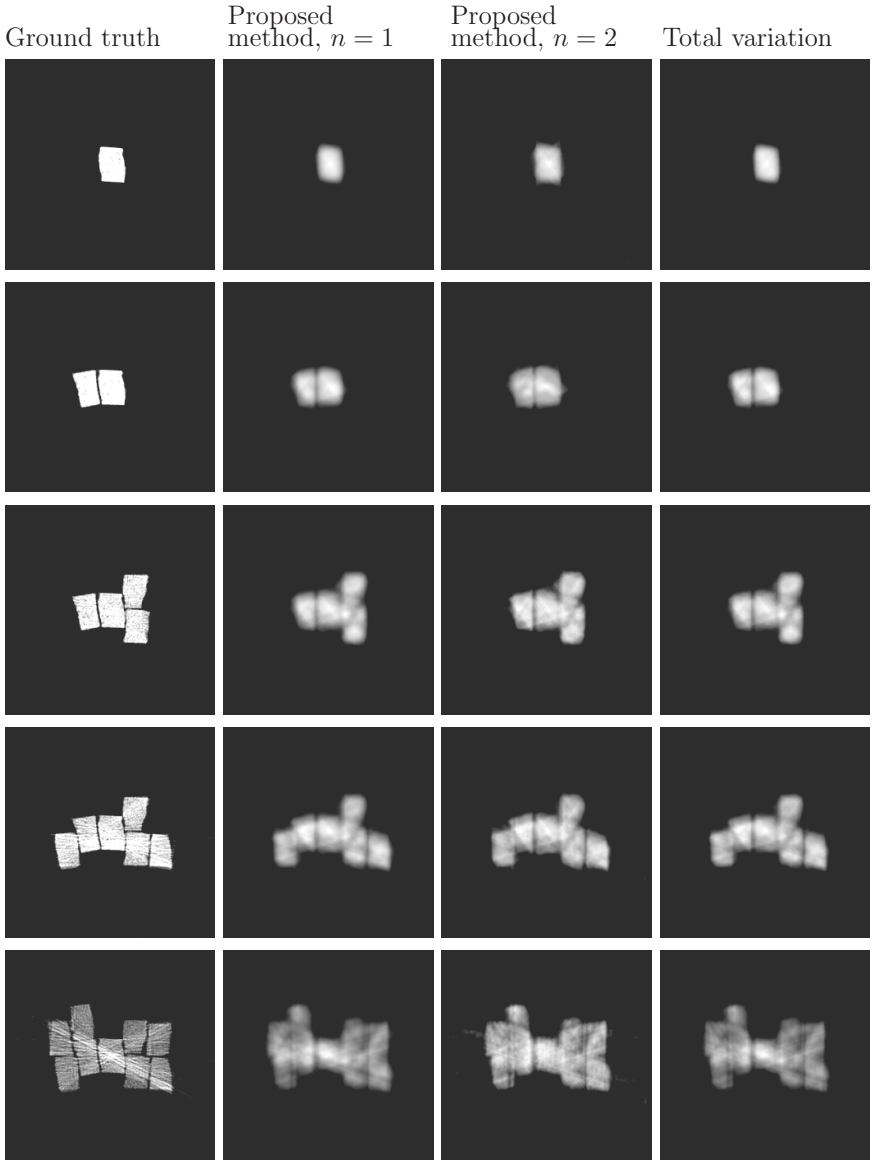

Figure 10: First five reconstructions of the dynamic sugar cube phantom. The number of projection images used in the reconstructions is ten (10) with 36 degree angular step. Spatial resolution 256×256.

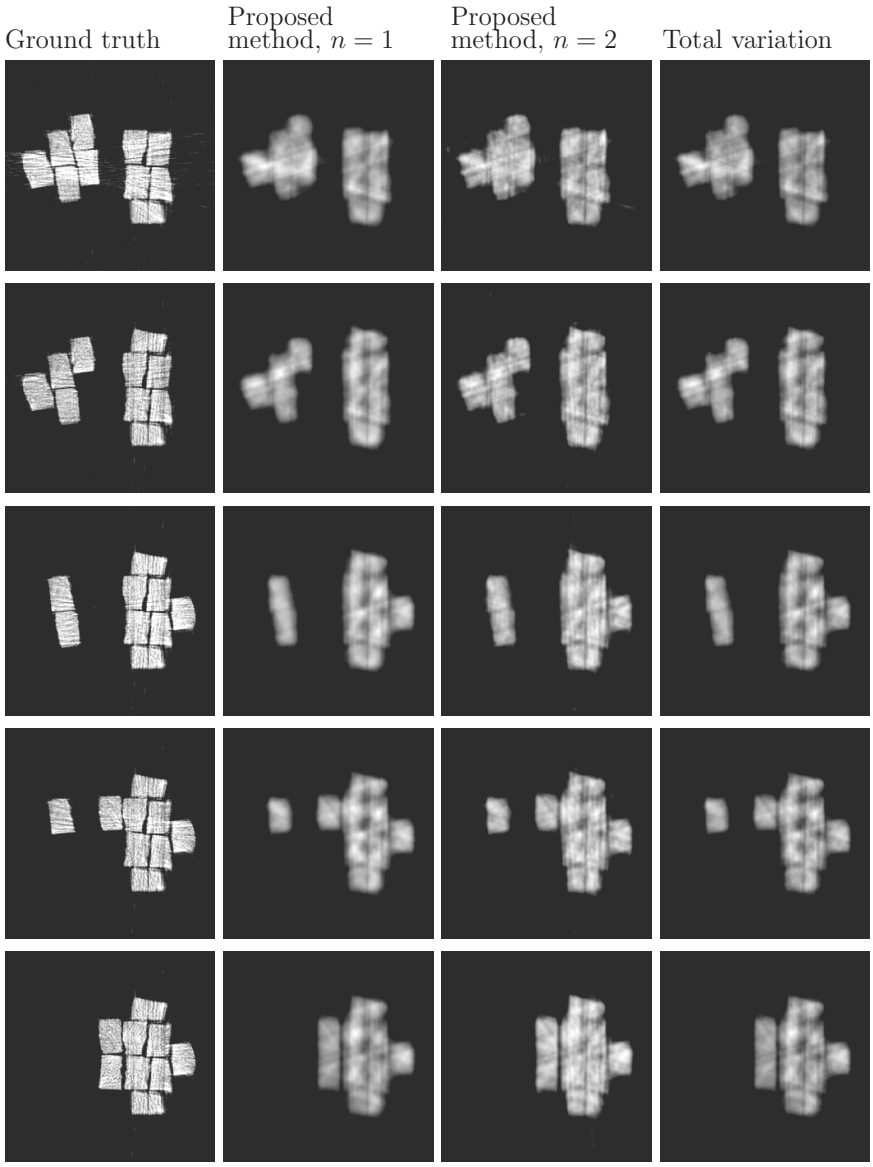

Figure 11: Last five reconstructions of the dynamic sugar cube phantom.

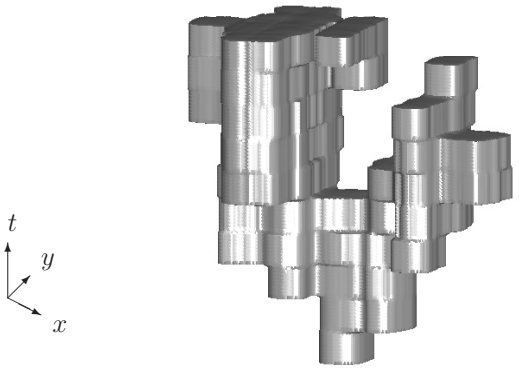

Figure 12: Isosurface image (in space-time) of the sugar cube reconstruction computed by the proposed modified space-time level set method with $n = 2$.

the indicator function

$$I_\omega(\tau) = \log \left| \int_\Gamma F(\varphi; d, k) g_N(-\varphi; \tau, k, \omega) d\sigma(\varphi) \right|, \quad \tau > 0. \tag{29}$$

Here, and throughout this section, we identify a point $\varphi = (\varphi_1, \varphi_2) \in S^1$ with the complex number $\varphi_1 + i\varphi_2$ and denote it by the same symbol. As mentioned in Section 6, in the full-aperture case $\Gamma = S^1$, the density g_N given by (12) and an appropriate choice of $\tau = \tau(N) \xrightarrow[N\to\infty]{} \infty$ gives the asymptotic relation

$$\frac{1}{\tau} I_\omega(\tau) \to h_D(\omega), \quad N \to \infty, \tag{30}$$

and in the limited-aperture case, i.e. Γ being a proper open subset of S^1, the corresponding limited-aperture density g_N can be given as a truncation of the formal solution of (14), see [24]. In Publication IV, the following explicit formula for the limited-aperture density was derived:

$$g_N(\varphi; \tau, k, \omega) = \sum_{m=0}^{N} \beta_m \varphi^m + \sum_{m=1}^{N} \beta_{-m} \overline{\varphi}^m, \quad \varphi \in -\Gamma, \tag{31}$$

where the set of coefficients β_m, $|m| \leq N$, is the unique solution of the linear system

$$G_N[\beta_{-N}, \ldots, \beta_{-1}, \beta_0, \beta_1, \ldots, \beta_N]^T = [\lambda^N, \ldots, \lambda, 1, \lambda^{-1}, \ldots, \lambda^{-N}]^T. \quad (32)$$

The matrix G_N is element-wise given by

$$\big[G_N\big]_{m,j} = \int_{-\Gamma} \varphi^m \varphi^j d\sigma(\varphi) = (\varphi^m, \varphi^{-j})_{L^2(-\Gamma)} \quad (33)$$

with $m = N, \ldots, -N$ and $j = -N, \ldots, N$, and

$$\lambda = \frac{(\tau + \sqrt{\tau^2 + k^2})\,\omega}{ik}. \quad (34)$$

The proposed algorithm for solving the inverse problem for a finite collection of directions $\omega \in S^1$ can now be formulated as follows.

1. Choose parameters $N \geq 1$ and $0 \leq \tau_1 < \tau_2 < \tau_3$.
2. Compute $I_\omega(\tau_j)$ for $j = 1, 2, 3$ using (29) and (31).
3. Fit a line to the points $(\tau_j, I_\omega(\tau_j))$ in the sense of least squares. Denote the slope of the line by $\widetilde{h}_D(\omega)$.
4. Approximate $h_D(\omega)$ by $\widetilde{h}_D(\omega)$.

We remark here again, that the theoretical result behind this approach ([24]) used the assumption that D is polygonal and the directions ω are regular with respect to D as explained in Section 6.

7.4.2 Numerical computations

Simulation of data. The synthetic data for numerical testing of the proposed algorithm was simulated using layer-potential presentation and boundary integral equations [12]. More precisely, the far field pattern (FFP) was computed as

$$F(\varphi; d, k) = \frac{e^{i\pi/4}}{\sqrt{8\pi k}} \int_{\partial D} e^{-ik\varphi\cdot y} f(y) ds(y), \quad (35)$$

where f was solved from the boundary integral equation

$$f(x) - 2\int_{\partial D} \frac{\partial \Phi(x-y)}{\partial \nu(x)} f(y) ds(y) = 2\frac{\partial}{\partial \nu} e^{ikx\cdot d}, \quad x \in \partial D, \quad (36)$$

with $\Phi(x) = \frac{i}{4}H_0^{(1)}(k|x|)$. Here $H_0^{(1)}$ is the Hankel function of the first kind and order zero. To obtain accurate data despite the (integrable) singularity of the kernel in the integral equation (36), a numerical quadrature similar to that in [35] was used for solving f from the resulting linear system of equations. Then simply a trapezoidal rule was applied for the evaluation of the far field pattern. Noisy data was simulated by adding 1% Gaussian random noise

$$\frac{0.01}{\sqrt{2}}(\epsilon_1 + i\epsilon_2)\max_{\varphi_\ell}|F(\varphi_\ell; d, k)|$$

to each value $F(\varphi_\ell; d, k)$ of the far field pattern. Here $\epsilon_1, \epsilon_2 \sim \mathcal{N}(0, 1)$ are normally distributed random numbers with mean zero and unit variance.

We remark that (36) may fail to be uniquely solvable for certain choices of D and k, which can lead to numerical difficulties. These situations were avoided in the numerical simulations by trial and error.

Computation of the support function. We follow the algorithm (steps 1–4) presented in the previous subsection (Sec. 7.4.1) with the following notes. The integral in the quantity

$$I_\omega(\tau_j) = \log\left|\int_\Gamma F(\varphi; d, k)g_N(-\varphi; \tau_j, k, \omega)d\sigma(\varphi)\right|, \quad j = 1, 2, 3,$$

was approximated by the sum

$$\frac{\text{length}(\Gamma)}{p}\sum_{\ell=1}^{p} F(\varphi_\ell; d, k)g_N(-\varphi_\ell; \tau_j, k, \omega)$$

with p uniformly distributed points φ_ℓ on Γ. The values of the density g_N were computed using (31). For this, we first formed the matrix G_N and the vector λ in equation (32) and solved for the coefficients β. Since the matrix G_N becomes ill-conditioned for small apertures Γ, we used truncated singular value decomposition with truncation level 10^{-6} to regularize the equation.

We remark that the proposed algorithm consists of numerical integration quadratures, solution of a (small) system of linear equations and standard least squares fitting. Hence, the inversion method is inexpensive computationally.

7.4.3 Numerical results

Let us then look at the numerical results in Figures 13 and 14. The original obstacles are shown by black curves while the gray areas depict the reconstructed convex hulls computed by the proposed algorithm. In Figure 13 the apertures Γ are half of the full circle while in Figure 14 the apertures are $1/4$ of the full circle. The directions ω were chosen to be 16 uniformly distributed vectors on S^1 and the wavenumber $k = 1$. For all the obstacles D the number of discretization points on the boundary was 600, with more dense grid near the possible corners of ∂D to enable better convergence.

The numerical results suggest that the proposed algorithm approximately recovers the convex hulls of obstacles from noisy limited-aperture far field data.

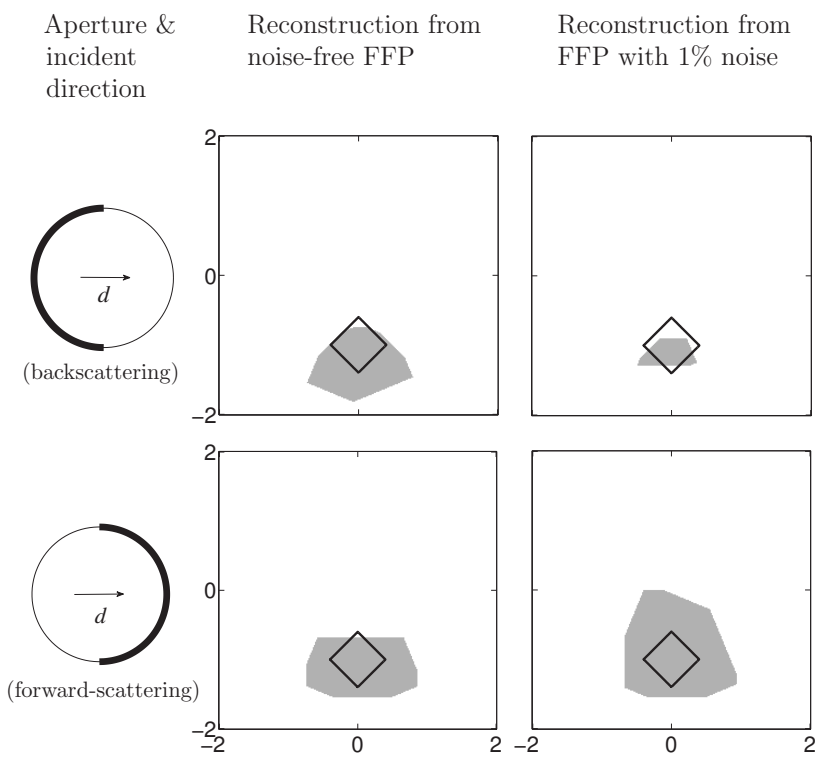

Figure 13: Polygonal sound-hard obstacle and limited-aperture data. First column: the apertures $\Gamma \subset S^1$ indicated by the bold parts of the circles, and the incident direction $d = (1, 0)$ shown inside the circles. Second and third column: reconstructions for each aperture from ideal and noisy data, respectively. Gray areas depict the computed convex hulls, and black curves indicate the correct boundary of the obstacle. The number of discretization points on Γ is 256. The values of the parameters are $N = 4$ and $\tau = 0, 0.5, 1$.

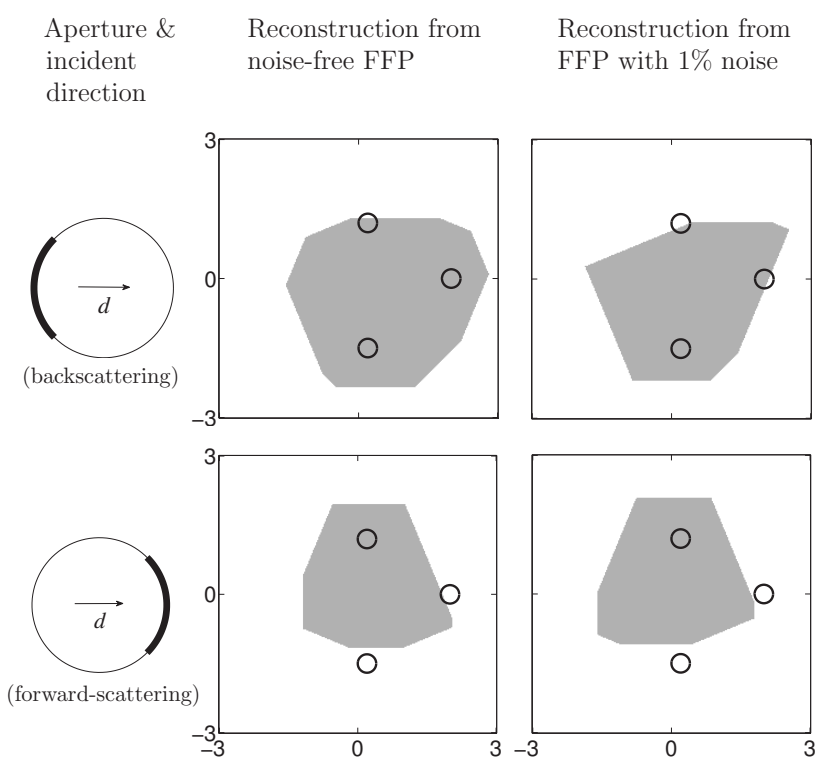

Figure 14: Smooth sound-hard obstacle and limited-aperture data. First column: the apertures $\Gamma \subset S^1$ indicated by the bold parts of the circles, and the incident direction $d = (1, 0)$ shown inside the circles. Second and third column: reconstructions for each aperture from ideal and noisy data, respectively. Gray areas depict the computed convex hulls, and black curves indicate the correct boundary of the obstacle. The number of discretization points on Γ is 128. The values of the parameters are $N = 4$ and $\tau = 0, 0.5, 1$.

References

[1] R. Acar and C. R. Vogel, *Analysis of total variation penalty methods*, Inverse Problems **10** (1994), 1217–1229.

[2] S. Bartels, *Total variation minimization with finite elements: Convergence and iterative solution*, SIAM Journal on Numerical Analysis **50** (2012), no. 3, 1162–1180.

[3] J. Barzilai and J.M. Borwein, *Two-point step size gradient methods*, IMA Journal of Numerical Analysis **8** (1988), no. 1, 141–148.

[4] M. Bertalmio, V. Caselles, B. Rouge, and A. Solé, *TV based image restoration with local constraints*, Journal of Scientific Computing **19** (2003), no. 1-3, 95–122.

[5] M. Burger, *A level set method for inverse problems*, Inverse Problems **17** (2001), no. 5, 1327–1355.

[6] Jian-Feng Cai, Stanley Osher, and Zuowei Shen, *Linearized Bregman iterations for frame-based image deblurring*, SIAM J. Imaging Sci. **2** (2009), no. 1, 226–252. MR 2486529 (2010h:94041)

[7] A. Chambolle and P. Lions, *Image recovery via total variation minimization and related problems*, Numerische Mathematik **76** (1995), 167–188.

[8] T. F. Chan, G. H. Golub, and P. Mulet, *A nonlinear primal-dual method for total variation-based image restoration*, SIAM Journal on Scientific Computing **20** (1999), no. 6, 1964–1977.

[9] T. F. Chan and C. Wong, *Total variation blind deconvolution*, IEEE Transactions on Image Processing **7** (1998), no. 6, 370–375.

[10] Tony F. Chan and Ke Chen, *On a nonlinear multigrid algorithm with primal relaxation for the image total variation minimisation*, Numer. Algorithms **41** (2006), no. 4, 387–411. MR 2230852 (2007i:68121)

[11] David Colton and Andreas Kirsch, *A simple method for solving inverse scattering problems in the resonance region*, Inverse Problems **12** (1996), no. 4, 383–393. MR 1402098 (97d:35032)

[12] David Colton and Rainer Kress, *Inverse acoustic and electromagnetic scattering theory*, second ed., Springer-Verlag, Berlin, 1998. MR 99c:35181

[13] P. L. Combettes and J. Pesquet, *Image restoration subject to a total variation constraint*, IEEE Transactions on Image Processing **13** (2004), no. 9, 1213–1222.

[14] A. H. Delaney and Y. Bresler, *Globally convergent edge-preserving regularized reconstruction: an application to limited-angle tomography*, IEEE Transactions on Image Processing **7** (1998), no. 2, 204–221.

[15] O. Dorn and D. Lesselier, *Level set methods for inverse scattering*, Inverse Problems **22** (2006), R67–R131.

[16] Ernie Esser, Xiaoqun Zhang, and Tony F. Chan, *A general framework for a class of first order primal-dual algorithms for convex optimization in imaging science*, SIAM J. Imaging Sci. **3** (2010), no. 4, 1015–1046. MR 2763706

[17] Hettlich F., *On the uniqueness of the inverse conductive scattering problem for the Helmholtz equation*, Inverse Problems **10** (1994), 129–144.

[18] Xiaobing Feng and Andreas Prohl, *Analysis of total variation flow and its finite element approximations*, M2AN Math. Model. Numer. Anal. **37** (2003), no. 3, 533–556. MR 1994316 (2004f:65149)

[19] R. Fletcher, *On the Barzilai-Borwein method*, Optimization and Control with Applications, Applied Optimization, vol. 96, Springer US, 2005, pp. 235–256.

[20] Massimo Fornasier, Andreas Langer, and Carola-Bibiane Schönlieb, *A convergent overlapping domain decomposition method for total variation minimization*, Numer. Math. **116** (2010), no. 4, 645–685. MR 2721637 (2011g:65099)

[21] Massimo Fornasier and Carola-Bibiane Schönlieb, *Subspace correction methods for total variation and l_1-minimization*, SIAM J. Numer. Anal. **47** (2009), no. 5, 3397–3428. MR 2551200 (2011d:65150)

[22] Tom Goldstein and Stanley Osher, *The split Bregman method for L1-regularized problems*, SIAM J. Imaging Sci. **2** (2009), no. 2, 323–343. MR 2496060 (2010e:65087)

[23] G. T. Herman and R. Davidi, *Image reconstruction from a small number of projections*, Inverse Problems **24** (2008), no. 4, 045011.

[24] M. Ikehata, *The Herglotz wave function, the Vekua transform and the enclosure method*, Hiroshima Math. J. **35** (2005), 1–22.

[25] Masaru Ikehata, *Inverse scattering problems and the enclosure method*, Inverse Problems **20** (2004), 533–551.

[26] T. L. Jensen, J. H. Jørgensen, P. C. Hansen, and S. H. Jensen, *Implementation of an optimal first-order method for strongly convex total variation regularization*, BIT Numerical Mathematics **DOI: 10.1007/s10543-011-0359-8** (2011).

[27] A.C. Kak and M. Slaney, *Principles of computerized tomographic imaging*, IEEE Service Center, Piscataway, NJ (1988).

[28] Willi A Kalender, *X-ray computed tomography*, Physics in medicine and biology **51** (2006), no. 13, R29.

[29] A. Kirsch, *An introduction to the mathematical theory of inverse problems*, Springer-Verlag, New York, 1996. MR 99c:34023

[30] ———, *Characterization of the shape of a scattering obstacle using the spectral data of the far field operator*, Inverse problems **14** (1998), 1489.

[31] V. Kolehmainen, M. Lassas, K. Niinimäki, and S. Siltanen, *Sparsity-promoting Bayesian inversion*, Inverse Problems **28** (2012), no. 2, 025005.

[32] V. Kolehmainen, M. Lassas, and S. Siltanen, *Limited data X-ray tomography using nonlinear evolution equations*, SIAM Journal on Scientific Computing **30** (2008), no. 3, 1413–1429.

[33] V. Kolehmainen, S. Siltanen, S. Järvenpää, JP Kaipio, P. Koistinen, M. Lassas, J. Pirttilä, and E. Somersalo, *Statistical inversion for medical X-ray tomography with few radiographs: II. application to dental radiology*, Physics in Medicine and Biology **48** (2003), 1465–1490.

[34] V. Kolehmainen, A. Vanne, S. Siltanen, S. Järvenpää, J.P. Kaipio, M. Lassas, and M. Kalke, *Parallelized Bayesian inversion for three-dimensional dental X-ray imaging*, IEEE Transactions on Medical Imaging **25** (2006), no. 2, 218–228.

[35] Rainer Kress, *On the numerical solution of a hypersingular integral equation in scattering theory*, J. Comput. Appl. Math. **61** (1995), no. 3, 345–360.

[36] M. Lassas and S. Siltanen, *Can one use total variation prior for edge-preserving Bayesian inversion?*, Inverse Problems **20** (2004), 1537–1564.

[37] D. R. Luke and R. Potthast, *The no response test – a sampling method for inverse scattering problems*, SIAM J. Appl. Math. **63** (2003), 1292–1312.

[38] J.L. Mueller and S. Siltanen, *Linear and nonlinear inverse problems with practical applications*, SIAM, 2012.

[39] F. Natterer, *The mathematics of computerized tomography*, Classics in applied mathematics, vol. 32, SIAM, 2001.

[40] Yurii Nesterov, *Barrier subgradient method*, Math. Program. **127** (2011), no. 1, Ser. B, 31–56. MR 2776709 (2012b:90138)

[41] E. Niemi, *Projected Barzilai–Borwein method for total variation regularization with nonnegativity constraints*, Bachelor of science thesis, Tampere University of Technology, 2010.

[42] Stanley Osher, Martin Burger, Donald Goldfarb, Jinjun Xu, and Wotao Yin, *An iterative regularization method for total variation-based image restoration*, Multiscale Model. Simul. **4** (2005), no. 2, 460–489 (electronic). MR 2162864 (2006c:49051)

[43] Stanley Osher and Ronald Fedkiw, *Level set methods and dynamic implicit surfaces*, Applied Mathematical Sciences, vol. 153, Springer-Verlag, New York, 2003. MR 1939127 (2003j:65002)

[44] R. Potthast, J. Sylvester, and S. Kusiak, *A 'range-test' for determining scatterers with unknown physical properties*, Inverse Problems **19** (2003), 533 – 547.

[45] E.T. Quinto, *Singularities of the X-ray transform and limited data tomography in* $\mathbb{R}^2$ *and* $\mathbb{R}^3$, SIAM Journal on Mathematical Analysis **24** (1993), 1215–1215.

[46] Potthast R., *Stability estimates and reconstructions in inverse acoustic scattering using singular sources*, Jour. Comp. Appl. Math. (2000), no. 114, 247 – 274.

[47] Marcos Raydan, *The Barzilai and Borwein gradient method for the large scale unconstrained minimization problem*, SIAM Journal on Optimization **7** (1997), no. 1, 26–33. MR 1430555 (98b:90131)

[48] R. A. Robb, Hoffman E. A., Sinak L. J., Harris L. D., and Ritman E. L., *High-speed three-dimensional x-ray computed tomography: the dynamic spatial reconstructor*, Proceedings of IEEE **71** (1983), no. 3, 308–319.

[49] L.I. Rudin, S. Osher, and E. Fatemi, *Nonlinear total variation based noise removal algorithms*, Physica D: Nonlinear Phenomena **60** (1992), no. 1-4, 259–268.

[50] F. Santosa, *A level set approach for inverse problems involving obstacles*, ESAIM Control Optimisation and Calculus of Variations **1** (1996), 17–33.

[51] Emil Y Sidky and Xiaochuan Pan, *Image reconstruction in circular cone-beam computed tomography by constrained, total-variation minimization*, Physics in Medicine and Biology **53** (2008), no. 17, 4777.

[52] G. M. Stiel, L. S. G. Stiel, E. Klotz, and C. A. Nienaber, *Digital flashing tomosynthesis: a promising technique for angiocardiographic screening*, IEEE Transactions on Medical Imaging **12** (1993), no. 2, 314–3321.

[53] Jie Tang, Brian E Nett, and Guang-Hong Chen, *Performance comparison between total variation (TV)-based compressed sensing and statistical iterative reconstruction algorithms*, Physics in Medicine and Biology **54** (2009), no. 19, 5781.

[54] Zhen Tian, Xun Jia, Kehong Yuan, Tinsu Pan, and Steve B Jiang, *Low-dose CT reconstruction via edge-preserving total variation regularization*, Physics in Medicine and Biology **56** (2011), no. 18, 5949.

[55] C.R. Vogel and M.E. Oman, *Fast, robust total variation-based reconstruction of noisy, blurred images*, IEEE Transactions on Image Processing **7** (1998), no. 6, 813–824.

[56] Wotao Yin, Stanley Osher, Donald Goldfarb, and Jerome Darbon, *Bregman iterative algorithms for l_1-minimization with applications to compressed sensing*, SIAM J. Imaging Sci. **1** (2008), no. 1, 143–168. MR 2475828 (2010f:90170)

[57] Xiaoqun Zhang, Martin Burger, and Stanley Osher, *A unified primal-dual algorithm framework based on Bregman iteration*, J. Sci. Comput. **46** (2011), no. 1, 20–46. MR 2753250